Feasibility study on inverse four-dimensional dose reconstruction using the continuous dose-image of EPID

Inhwan Jason Yeo[a)]
Radiation Medicine Program, Loma Linda University Medical Center, Loma Linda, California 92354

Jae Won Jung
Department of Physics, East Carolina University, Greenville, North Carolina 27858

Byong Yong Yi
Radiation Oncology, University of Maryland School of Medicine, Baltimore, Maryland 21201

Jong Oh Kim
Department of Radiation Oncology, University of Pittsburgh Cancer Institute, Pittsburgh, Pennsylvania 15232

(Received 11 October 2012; revised 22 February 2013; accepted for publication 21 March 2013; published 10 April 2013)

Purpose: When an intensity-modulated radiation beam is delivered to a moving target, the interplay effect between dynamic beam delivery and the target motion due to miss-synchronization can cause unpredictable dose delivery. The portal dose image in electronic portal imaging device (EPID) represents radiation attenuated and scattered through target media. Thus, it may possess information about delivered radiation to the target. Using a continuous scan (cine) mode of EPID, which provides temporal dose images related to target and beam movements, the authors' goal is to perform four-dimensional (4D) dose reconstruction.
Methods: To evaluate this hypothesis, first, the authors have derived and subsequently validated a fast method of dose reconstruction based on virtual beamlet calculations of dose responses using a test intensity-modulated beam. This method was necessary for processing a large number of EPID images pertinent for four-dimensional reconstruction. Second, cine mode acquisition after summation over all images was validated through comparison with integration mode acquisition on EPID (IAS3 and aS1000) for the test beam. This was to confirm the agreement of the cine mode with the integrated mode, specifically for the test beam, which is an accepted mode of image acquisition for dosimetry with EPID. Third, in-phantom film and exit EPID dosimetry was performed on a moving platform using the same beam. Heterogeneous as well as homogeneous phantoms were used. The cine images were temporally sorted at 10% interval. The authors have performed dose reconstruction to the in-phantom plane from the sorted cine images using the above validated method of dose reconstruction. The reconstructed dose from each cine image was summed to compose a total reconstructed dose from the test beam delivery, and was compared with film measurements.
Results: The new method of dose reconstruction was validated showing greater than 95.3% pass rates of the gamma test with the criteria of dose difference of 3% and distance to agreement of 3 mm. The dose comparison of the reconstructed dose with the measured dose for the two phantoms showed pass rates higher than 96.4% given the same criteria.
Conclusions: Feasibility of 4D dose reconstruction was successfully demonstrated in this study. The 4D dose reconstruction demonstrated in this study can be a promising dose validation method for radiation delivery on moving organs. [http://dx.doi.org/10.1118/1.4799941]

Key words: four-dimensional dose reconstruction, continuous scan, EPID

I. INTRODUCTION

For the treatment of a moving organ various delivery and planning techniques have been developed to reduce an internal margin while not compromising tumor control.[1–9] All of these advancements have been made possible by assuming reasonably accurate real-time acquisition of patient's target movement by using external surrogates (respiratory gated radiation therapy) or internally implanted markers (motion adaptive delivery).[10–13] Regarding this assumption, however, the accuracy of the real-time acquisition and thus that of planned adaptive delivery remains to be confirmed. This is because a patient's internal organ may exhibit movement which is not detectable by external surrogates due to baseline shift and other changes in the respiratory traces of a patient.[14,15] Such movement involves geometrical changes as well as density changes of calculation voxels of target and neighboring organs, compared with conditions of patients' anatomy at the time of treatment planning, thereby leading to differences in dose delivery. In addition to the above considerations, interplay of dynamic IMRT delivery and lung motion has been reported to cause differences in delivered dose.[16,17] As a quality

assurance measure, therefore, retrospective verification of such deliveries on moving organs might be necessary.[18]

The transit radiation dosimetry in electronic portal imaging device (EPID) is a well-documented method of dose validation.[19–22] Images in EPID represent the irradiated beam that has undergone attenuation through the target organ. This idea can be utilized for the case of moving beam and organs. Through the continuous (cine) imaging in EPID, the recorded images, in principle, represent the beam (position and output) attenuated through the organ (position). In support of this idea, the continuous dose imaging of exit radiation by EPID was recently demonstrated with sufficient dosimetric accuracy by McCurdy and Greer.[23] Han-Oh *et al.*[24] demonstrated the feasibility of using EPID images to determine the geometrical accuracy of tumor tracking treatment with a moving MLC system.

The continuous transit images using EPID (Ref. 23) can be utilized for reconstructing dose in a patient, provided that 4D anatomical information representative of patient's treatment position is acquired.[26] Such 4D imaging was demonstrated by a four-dimensional cone-beam CT (4D CBCT) introduced by Sonke *et al.*[26] While it remains to be answered whether or not the 4D imaging is made possible during radiation delivery to the patient, thereby acquiring representative anatomical information of a patient during treatment, this is beyond the scope of this study. This study is intended to test on the feasibility of the 4D dose reconstruction from transit imaging as a first attempt. To our knowledge, no report exists on the 4D dose reconstruction in a patient performed inversely from transit images.

Therefore, this study aimed at proposing and validating the 4D dose reconstruction. To achieve this aim, we first introduced a method of generalized dose response suitable for the 4D dose reconstruction that involves the number of reconstruction processes equivalent to the number of cine images. We later developed a program to apply the method for 4D dose reconstruction on phantoms and validated the method.

II. MATERIALS AND METHODS

II.A. Dose reconstruction method based on responses to virtual beamlets

The method of dose reconstruction we have developed in our prior study utilizes dose responses to unit virtual beamlet intensities in phantom and EPID.[25] The virtual beamlet was previously defined as a unit field opening with a small size (for example, 0.5 × 0.5 cm). Thus, the entire opening of a beam segment is occupied by multiple unit field openings, and thus virtual beamlets. To review the method, we first describe doses deposited in EPID and phantom mathematically. The virtual beamlet dose response in EPID, $\underline{\underline{R_e}}(t)$, at time t, when multiplied (i.e., superposition) with virtual beamlet intensity at time t, $\underline{I}(t)$, generates the dose deposited in EPID at time t, $\underline{E}(t)$, as shown in Eq. (1):

$$\underline{E}(t) = \underline{\underline{R_e}}(t) \cdot \underline{I}(t). \tag{1}$$

Similarly, the virtual beamlet dose deposited in phantom $\underline{P}(t)$ is derived in Eq. (2):

$$\underline{P}(t) = \underline{\underline{R_p}}(t) \cdot \underline{I}(t), \tag{2}$$

where $\underline{\underline{R_p}}(t)$ is the virtual beamlet dose response in the phantom. From Eqs. (1) and (2), we derive Eq. (3):

$$\underline{P}(t) = \underline{\underline{R_p}}(t) \cdot [\underline{\underline{R_e}}(t)^{-1} \cdot \underline{E}(t)]. \tag{3}$$

Equation (3) shows linear relationship between the responses $\underline{\underline{R_e}}(t)$ and $\underline{\underline{R_p}}(t)$ and between the doses $\underline{E}(t)$ and $\underline{P}(t)$, respectively.[25] Note that Eqs. (1)–(3) are exact in the computational sense, employing calculated values for each term. After the responses of all virtual beamlets with unit intensities that fills the field opening (i.e., beam segment, if IMRT) were acquired by Monte Carlo calculation on the given phantom and EPID models, the responses were then used to establish the relationship in Eqs. (1) and (2). A more detailed description is given in our prior study.[25]

When actual radiation delivery with a particular intensity map (MLC positions and beam segment output) occurs, in Eqs. (1) and (3), $\underline{E}(t)$ is replaced with a measurement value $\underline{E}'(t)$; $\underline{P}(t)$ with deposited dose $\underline{P}'(t)$; $\underline{\underline{R_e}}(t)$ and $\underline{\underline{R_p}}(t)$ by the measured responses to the virtual beamlets within delivered segments $\underline{\underline{R_e}}'(t)$ and $\underline{\underline{R_p}}'(t)$, respectively. Equation (3) can then be written as

$$\underline{P}'(t) = \underline{\underline{R_p}}'(t) \cdot [\underline{\underline{R_e}}'(t)^{-1} \cdot \underline{E}'(t)]. \tag{4}$$

This equation is exact in the experimental sense with each term representing actual delivery. By replacing $\underline{E}(t)$ in Eq. (3) with a measurement value $\underline{E}'(t)$, deposited dose $\underline{P}'(t)$ from actual delivery is reconstructed. The accuracy of the reconstruction relies on that of the calculated responses $\underline{\underline{R_e}}(t)$ and $\underline{\underline{R_p}}(t)$ in predicting actual delivery (i.e., measurements) in terms of responses $\underline{\underline{R_e}}'(t)$ and $\underline{\underline{R_p}}'(t)$.

When we apply the above method of dose reconstruction to 4D cases, we face computational challenges. With our method of dose reconstruction,[25] Eq. (3) has been designed to be used for the given MLC (i.e., beam segments) and patient positions involved in IMRT delivery. This implies that the responses $\underline{\underline{R_e}}(t)$ and $\underline{\underline{R_p}}(t)$ have to be calculated for virtual beamlets in every beam-segment aperture of an IMRT beam which changes with time until the assigned MU delivery is completed. In addition to this effort, the temporal dose reconstruction involves additional consideration of changes in patient positions with time. This approach necessitates as many calculations as the number of combinatory positions of a moving phantom and a beam aperture, thus requiring significant computational resources. In order to avoid this, our method of dose reconstruction was adapted to use the response to virtual beamlets under a jaw opening (defined by jaws that enclose the MLC apertures of an IMRT beam) when we reconstruct the deposited dose in phantom for delivered beam intensities (defined by delivered MLC-shaped apertures). Such responses are more generalized as they are not specific to a beam aperture shape, and are applicable to any beam aperture

enclosed within the jaw opening. These generalized responses save us from considering the variable component of temporal beam changes; only phantom position changes need to be considered.

To describe the new method mathematically, let us first write equations similar to Eqs. (1)–(3) employing virtual beamlet dose response in EPID and phantom under the jaw opening, $\underline{\underline{R_e^g}}$ and $\underline{\underline{R_p^g}}$, respectively (i.e., generalized responses):

$$\underline{E} = \underline{\underline{R_e^g}} \cdot \underline{I}. \tag{5}$$

Similarly,

$$\underline{P} = \underline{\underline{R_p^g}} \cdot \underline{I}. \tag{6}$$

From Eqs. (5) and (6), we derive Eq. (7):

$$\underline{P} = \underline{\underline{R_p^g}} \cdot [\underline{\underline{R_e^{g^{-1}}}} \cdot \underline{E}], \tag{7}$$

where the time variable is removed, because there is no temporal change of a radiation field (aperture) by a jaw opening. This equation is exact in a computational sense.

Our goal for the new method is to avoid calculating the responses to the delivered virtual beamlets associated with IMRT delivery in Eq. (7) (not considering temporal beam change by MLC aperture change). To reach this goal, we can start by formulating equations similar to Eqs. (5) and (6) for delivered beamlets while we choose to keep the generalized responses unchanged. Then, we have the following expressions:

$$\underline{E'}(t) \cong \underline{\underline{R_e^g}} \cdot \underline{I}^p(t), \tag{8}$$

$$\underline{P'}(t) \cong \underline{\underline{R_p^g}} \cdot \underline{I}^p(t), \tag{9}$$

where $\underline{I}^p(t)$ is the pseudo-delivered virtual beamlet intensity, not an actual delivered intensity, that is defined to approximate the equality. If the responses to the delivered beamlets $\underline{\underline{R_e}'}(t)$ and $\underline{\underline{R_p}'}(t)$ and the delivered beamlet intensity $\underline{I}'(t)$ were used in Eqs. (8) and (9), the two equations would be exact [restoring Eq. (4)]. As the generalized responses were used, in order to approximate the equality $\underline{I}^p(t)$ was defined. Note that the equality can only be approximated, because Eqs. (8) and (9) are matrix formulations consisting of multiple linear equations. From Eqs. (8) and (9), we derive Eq. (10):

$$\underline{P'}(t) \cong \underline{\underline{R_p^g}} \cdot \left[\underline{\underline{R_e^{g^{-1}}}} \cdot \underline{E'}(t)\right]. \tag{10}$$

Equation (10) becomes exact [it becomes Eq. (4)] when the equality exists between the response ratio operators, $\underline{\underline{R_p^g}} \cdot [\underline{\underline{R_e^{g^{-1}}}} \cdot \_]$ and $\underline{\underline{R'_p}}(t) \cdot \lfloor \underline{\underline{R'_e}}(t)^{-1} \cdot \_ \rfloor$ of the jaw and MLC segment openings, respectively, as shown in Fig. 1. The equality in Eq. (10) is an approximation as much as the equality between the response ratios is approximate. However, the inaccuracy associated with this relation is smaller than that of each response by an order of magnitude due to the use of response "ratio" [i.e., superposition of $\underline{\underline{R_e}}(t)$ and $\underline{\underline{R_p}}(t)^{-1} \cdot]$ rather than responses. In more detail, the difference between

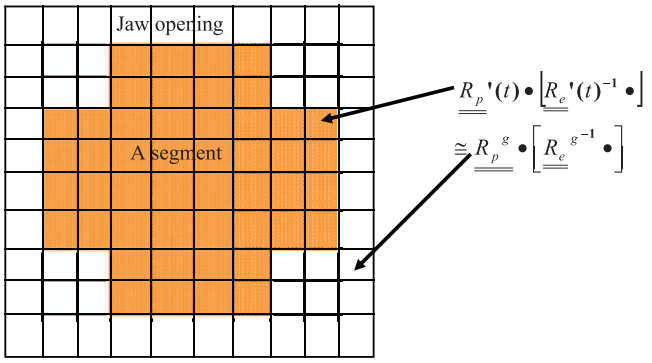

FIG. 1. Response ratio operator of virtual beamlet under jaw opening that replaces the response ratio of delivered beamlet under beam segments (colored).

$\underline{\underline{R_p^g}}$ and $\underline{\underline{R_p}}$ is as obvious as the difference between irradiated doses from a jaw opening and a shaped MLC aperture, respectively. However, the difference between the ratio-like quantities such as $\underline{\underline{R_p^g}} \cdot [\underline{\underline{R_e^{g^{-1}}}} \cdot \_]$ and $\underline{\underline{R'_p}}(t) \cdot \lfloor \underline{\underline{R'_e}}(t)^{-1} \cdot \_ \rfloor$ of the two openings, respectively, is not as obvious. This mathematical trend was later proven by the good pass rates of the validation experiments (results). Furthermore, a finite phase (i.e., ten temporal phases) of phantom images was utilized in this study. As such time-approximate images were used to represent patient's position on which responses were calculated for 4D dose reconstruction, the response ratio calculations could be approximated as well. This new method does eliminate the need of modeling the dynamic (temporal) beam component for response calculation; only the moving positions of the phantom of concern need to be considered. In the following study, this derivation has been first validated and the four-dimensional dose reconstruction using the method has been performed.

II.B. Phantom imaging

In order to validate the above method and to perform the 4D dose reconstruction, phantoms were prepared and imaged. A homogeneous phantom was placed on a movable (but kept static) platform as shown in Fig. 2(a) and was imaged with CT. Even if it was to be used for the 4D dose reconstruction, four-dimensional imaging would not be necessary as the phantom does not contain any heterogeneity, and thus is invariable over time. The homogeneous phantom consisted of two 5 cm-thick slabs. To prepare a heterogeneous phantom, the 5-cm thick heterogeneous slab shown in Figs. 2(b) and 2(c) was prepared with a drilled pyramid-shape hole within it. With the hole facing upward, the slab was placed on top of a homogeneous 5-cm thick slab to constitute a heterogeneous phantom as a combination. The isocenter was placed at the center of the hole for the heterogeneous phantom and at the mid depth (5 cm) of the two phantoms that were placed above the platform at the base position. The hole-structure in the heterogeneous phantom effectively provided heterogeneity (lung/tissue) suitable for this study. Temporal imaging of the heterogeneous phantom was

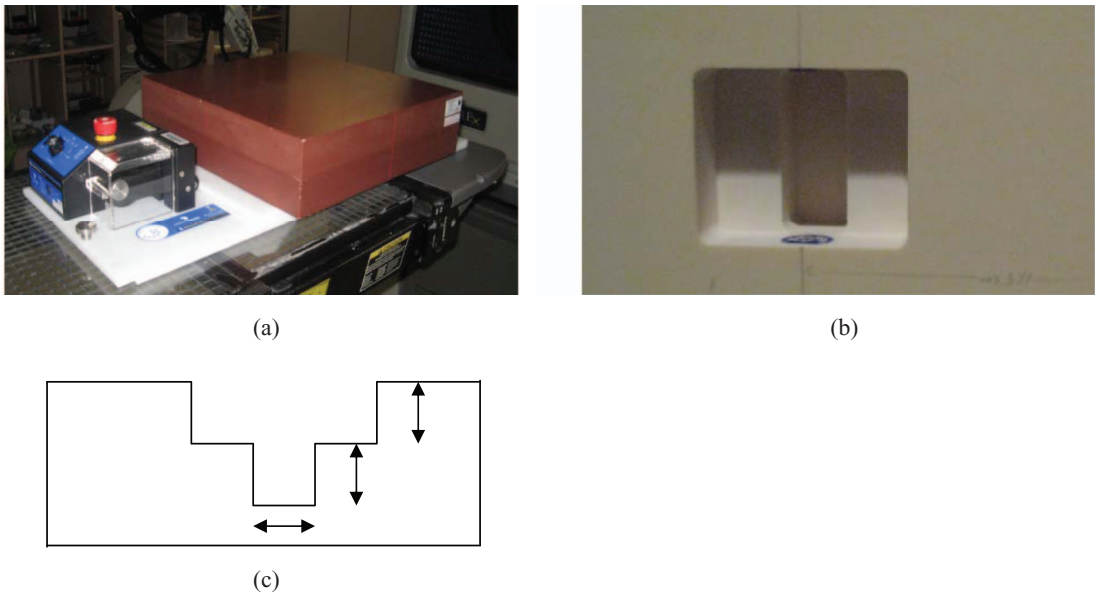

FIG. 2. Measurement setup. (a) Film is sandwiched in the middle of the two 5 cm solid water phantoms on a moving platform. (b) The top view of the top slab that has a cavity. (c) A cavity in (b) cross-sectional view. Each distance in the cavity is 2 cm. The phantom moved horizontally along in-plane.

done while the platform was moving with a period of 4.5 s over a distance of 4 cm. The 4D CT images were sorted in terms of phases at 10% interval. The acquired images were used for dose calculations in phantom and EPID throughout this study.

II.C. Reconstruction method validation

For the validation of the method, a test beam was designed and used to irradiate the 10 cm-thick flat phantom and EPID. The dose reconstruction was then performed from EPID images and compared with in-phantom film measurement.

II.C.1. Test beam

The test beam was composed of three (in x-direction; step-and-shoot), columnar irradiations shaped by MLC (see Fig. 3). The first segment was 3 cm wide and was spaced between 4.5 (X2) and 1.5 cm (X1); the second was 6 cm wide and was spaced between 4.5 (X2) and −1.5 cm (X1); the third was 9 cm wide and was spaced between 4.5 (X2) and −4.5 cm (X1). The collimator was rotated by 90°, so that the segment change was done along the in-plane direction. Weightings of the three segments were equally distributed. This created a half-pyramid-shape beam irradiated by a step-and-shoot manner. The test beam with 6 MV at 300 MU/min and a total delivery of 80 MU was used throughout this study.

II.C.2. Measurements

For EPID measurements, the image calibration of aS1000 EPID was first carried out to correct for variant pixel outputs. A flood field (an open beam of 22 × 17 cm^2) flattened under a 10 cm-thick solid water phantom (95.0 cm SSD) was used to irradiate EPID. The device was positioned at a relatively large distance of 183 cm. In this setup, the flat beam profile can uniformly cover the imager.[27] After the image calibration, the dose calibration of EPID images was performed, creating a dose calibration matrix between the measured image of the flat flood field to the corresponding calculated dose image using the EPID model described in our other study.[28] After the calibration, the test beam was irradiated on the 10-cm thick homogeneous phantom [Fig. 2(a)] and EPID that was placed at 150 cm. The measured pixel number of EPID was converted to dose using the acquired calibration matrix. All measurements in this section were done on the integration mode of image acquisition in EPID.

During the test beam irradiation, in-phantom film dosimetry was concurrently performed at the mid plane of the phantom, in between the two slabs shown in Fig. 2(a). For film dosimetry, calibration measurements were performed at the

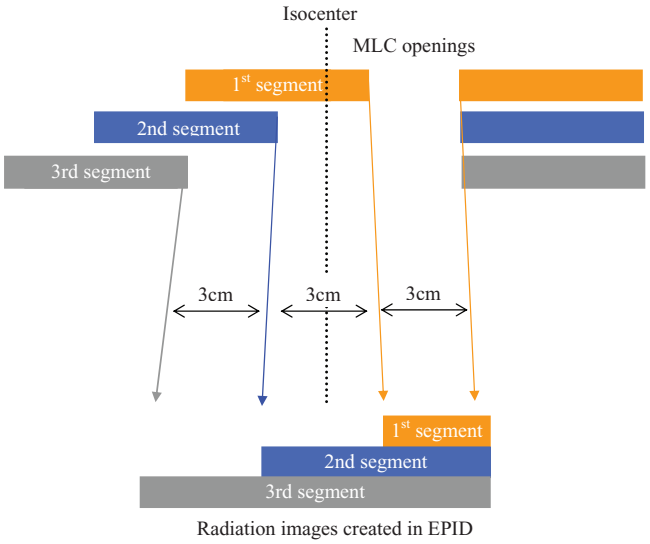

FIG. 3. A test IMRT beam used in this study.

same measurement condition (phantom and depth) using a 6 MV X-ray beam, the field size of 6 × 6 cm^2, and monitor units ranging from 0 to 100 at the interval of 10 MUs.[25,29] The X-Omatic V (XV) film was used and developed by Kodak X-OMAT 2000A processor, read by a scanner (Dosimetry pro, Vidar, Herndon, VA, US), and digitized by RIT114 system (RIT, Colorado Springs, CO, US). The calibration curve was derived based on the two sets of data: one is net optical densities and the other is dose calculated by the XVMC code at the calibration condition (i.e., measurement depth and field size) in the scanned phantom images.[30] The Monte Carlo calculation was used because the dose calibration of EPID image was against the calculated dose image, as discussed above, which is based on a nominal output (not daily fluctuated output). The in-phantom dose was reconstructed from the dose-calibrated EPID image, and then compared with the in-phantom film. Therefore, the film needed to be calibrated against a nominal output as calculated at the same measurement condition, provided that the Monte Carlo code was accurate within 1% error from ion chamber measurement in our prior work.[25] Our approach was to validate the method of dose reconstruction. However, for application, EPID images can be calibrated against a daily fluctuated dose (considered in the Monte Carlo EPID model). The measured film image of the test beam was filtered using a median filter (5 × 5 pixels) by the film evaluation system (Radiologic Imaging Technology, Colorado Springs, CO) to reduce noise in the film data with fine resolution (0.178 mm) and converted into dose using the acquired calibration curve.

II.C.3. Dose reconstruction

Dose responses were calculated for dose reconstruction. For the response calculation, the scanned phantom images obtained previously were transferred into the XVMC code.[30] Behind the scanned images in the code, we have placed our EPID model. We have calculated the virtual beamlet dose responses $\underline{\underline{R_e^g}}$ and $\underline{\underline{R_p^g}}$ with the unit beamlet size of 0.5 × 0.5 cm^2 sampled across the open beam (10 × 10 cm^2) in the homogeneous flat phantom and the EPID using the code. The calculations were performed at the resolution of 0.25 × 0.3 × 0.25 cm^3 in the phantom which can provide statistically significant calculation results (<3% uncertainty). Varian 120 leaf MLC modeling in XVMC, which contains tongue-and-groove and rounded leaf tip modeling, was used. The couch was not modeled in this study, but the predetermined amount of attenuation (2.5% from our measurements in EPID with and without couch) was considered. Using the acquired responses and the EPID image of the test beam [in Eq. (10)], we have performed dose reconstruction in the mid plane of the phantom and compared it with the film measurement. The dose in the same plan was also forwardly calculated.

II.D. 4D dose reconstruction

II.D.1. Validation of EPID cine imaging

Four-dimensional dose reconstruction requires 4D (i.e., temporal or cine) EPID imaging. Although the cine mode acquisition on EPID (IAS3 and aS1000) was documented as a reliable mode of image acquisition by McCurdy and Greer,[23] it was validated specifically for the test beam in this study. The latter was done because McCurdy and Greer validated the cine imaging for sliding-window beams only, while our test beam is a step-and-shoot beam. In more detail, step and shoot beams involve different temporal characteristics of MLC travel from a sliding-window beam. The EPID imaging captures signals time-dependently through horizontal and longitudinal scans across EPID. Furthermore, such temporal nature can also be affected by the model of EPID and the associated acquisition software system (that affect the speed and stability of scan) and the condition of a linear accelerator such as dose rate stability.[23] Therefore, the test beam needed to be validated. For validation, we have compared a summed image of cine images over time with images acquired in the integration mode. The integration mode is an established mode of image acquisition for dosimetry with EPID, and thus the cine acquisition can be validated through this comparison. Various MUs from 10 to 200 were used to test the dependence of this comparison on delivered dose. No phantom was placed for this validation. For the cine mode, BeamOnDelay was set to 0 ms and the mode of Not-Synchronized-to-Beam-Pulses was chosen.[23]

II.D.2. Measurements

After the cine mode validation, 4D dose reconstruction from the cine images was performed and validated. That reconstruction process involved measurement and calculations of the above test beam. For measurement, in-phantom film dosimetry and EPID measurements using the cine mode were performed on the homogeneous and heterogeneous phantoms which were placed on a moving platform. Films were placed in the mid plane of the 10-cm thick phantoms and concurrently received irradiation while EPID image acquisition was performed. During irradiation, the phantom with film moved along the direction of in-plane with the period and distance used in imaging. In all four-dimensional measurements, the beam-on start was synchronized with the motion start of the platform (i.e., at the base position) manually by visual determination through a camera.

II.D.3. Dose reconstruction

For dose reconstruction, we have calculated virtual beamlet dose responses $\underline{\underline{R_e^g}}$ and $\underline{\underline{R_p^g}}$, from an open beam (10 × 10 cm^2) in moving homogeneous and heterogeneous phantoms film measurement plane and EPID. The dose responses were calculated for the heterogeneous phantom case for each phase. They were also calculated on the homogeneous phantom case only once for all phases. The XVMC code with calculational details described above were similarly used.

After measurements of the test beam, in-phantom dose was reconstructed from the EPID images for each phase (t) of the phantom move using Eq. (10). The phase-independent responses were used for the entire cine images for the

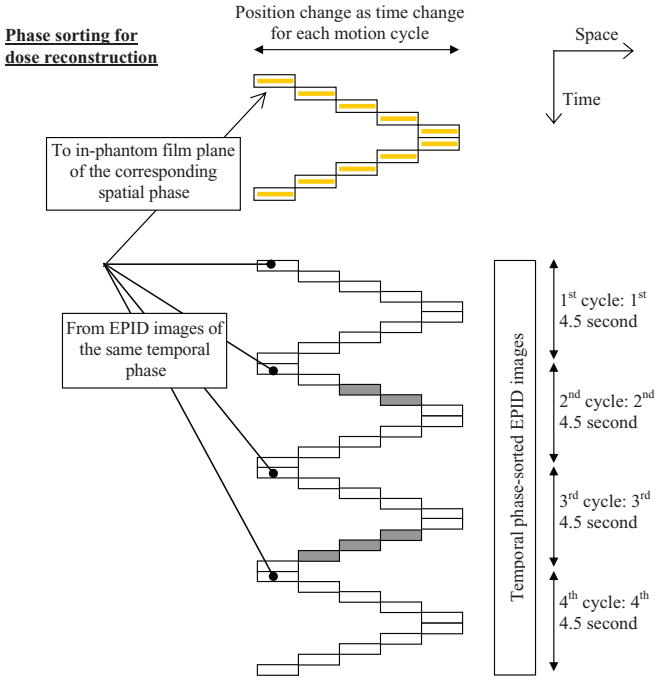

FIG. 4. Four-dimensional dose reconstruction diagram from EPID to phantom. EPID images were temporal phase-sorted and assigned to corresponding spatial phases. Darkened phases imply (partially) discontinued acquisition due to MLC travel between segments.

reconstruction in the homogenous phantom. For the heterogeneous case, the phase-specific responses were used for the corresponding phase-specific cine images. The process of dose reconstruction is described in Fig. 4. During the entire course of radiation delivery, the phantom moved four cycles approximately. The temporal and interrelated positional phases (10 phases) of the moving phantom imbedded with film (upper diagram) are graphically represented as shown in the figure. Note that although temporal phases were increasing until the end of dose delivery even after the first cycle, positional phases were repeating. Therefore, only 10 positional phases were depicted for the phantom. During these four cycles of movement, continuously scanned EPID images were acquired. They were then sorted at 10% temporal-phase interval (translated from 10% positional phase interval based on the ratio of 4.5 s/4.0 cm), thereby producing a total of 40 temporal phases. While the phantom motion is repetitive over four cycles, EPID images are not, due to the nature of the dynamic beam (MLC change), requiring all 40 phases. This is graphically represented in the diagram of four cycles next to the EPID image phases (i.e., phase-sorted images) in Fig. 4 with each cycle allotted with 10 phases. Among these phases, four temporal phases were correlated to each positional phase of the phantom (graphically, they were vertically related). As an example, if the reconstruction is done for the first 10% positional phase, then all images taken at this phase interval for each cycle were processed with the precalculated responses on the representative heterogeneous phantom image of the same phase interval (see the arrowed lines). Therefore, reconstruction calculations as many as the number of EPID images were performed for each phase. After such calculations, the reconstructed doses were summed for each phase. As a next step, the reconstructed dose for each phase was summed over all 10 phases considering the movement of the phantom: each reconstructed dose was assigned to the corresponding positional phase of the phantom. More details on the image sorting are explained in Sec. III. For the positional assignment, phase t and dimension variables x for a sinusoidally moving platform were related by Eq. (11),

$$x = x_0 + \frac{\boldsymbol{\alpha}}{2} \cdot \left(1 - \mathbf{cos}\left(\frac{2\boldsymbol{\pi} \cdot t}{p}\right)\right), \tag{11}$$

where α is the amplitude of the moving platform; p is the period of the moving platform; and x_0 is the coordinate of a static reference. The second term in the right-hand side is the travel distance of the phantom at time t. This equation was digitized into a finite set of data by a fixed interval (corresponding to a phase interval) and used for the positional assignment. The resultant distribution was compared with the dose that the in-phantom film has been receiving while moving, during the entire dose delivery, following the sinusoidal motion described by Eq. (11).

The four-dimensional dose from the test beam was forwardly calculated for comparison with the reconstructed dose. The process of phase sorting to construct the 4D dose was conceptually identical to that for the dose reconstruction (Fig. 4). For this process, $\underline{\underline{R_p}}(t)$ was calculated for each combination of beam apertures and phase-specific phantom images, and the phase-specific dose was calculated based on Eq. (2). In more detail, for $\underline{\underline{R_p}}(t)$ calculation the temporal phases of phantom were sorted similarly to the sorting of EPID images (Fig. 4). In the place of each phase-specific EPID images in Fig. 4, the dose was calculated for each phase in each corresponding phase-sorted images from each corresponding beam segment. The segment was assigned as follows. As the test IMRT beam consists of three segments with equal weights, a total of 40 temporal phases of phantom was equally divided into three groups. The phantom phase in the first 13.3 group received the irradiation from the first segment. The second (13.4–16.6) and the third (16.7–40) groups received the second and the third segments, respectively. If a certain phase was associated with a noninteger phase number such as the 13.3th phase after the 13th phase, all relevant beam segments (i.e., 1st and 2nd segments) were irradiated to the corresponding phase-specific images (4th phase) and the calculated response was determined by a ratio of contribution from the two segments (30% and 70%, respectively). Doses were similarly sorted into 10 phase-specific doses and summed using Eq. (11).

III. RESULTS AND DISCUSSIONS

III.A. Reconstruction method validation

Figure 5 compares the reconstructed dose profile (b) with the measured (a) and the forward MC-calculated (c) responses for the test beam on the static film and phantom. In the central profile comparison (d), the dose differences between (b) and (a) in the central points of the maximum, medium,

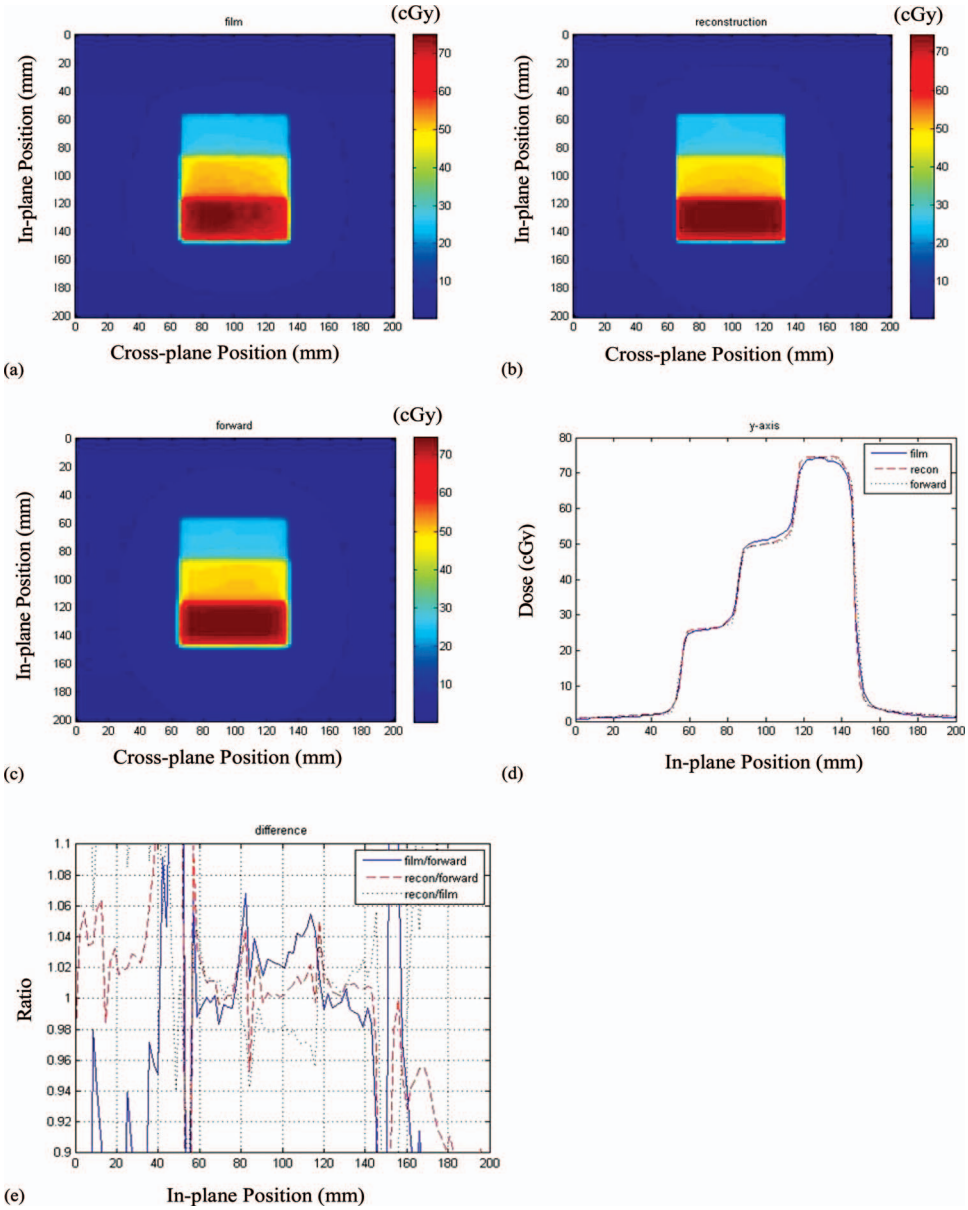

FIG. 5. (a) Dose profiles in cGy measured with film on a midplane in the flat phantom under no motion, (b) dose profiles reconstructed at the same condition, (c) dose profiles forward-calculated at the same condition, (d) central dose profile comparison between the three at X = 100 mm, (e) dose differences along the central in-planar direction.

and minimum shoulders were 1.0%, 2.0%, and 1.0%, respectively, as shown in Fig. 5(e). Two-dimensional dose comparison showed that 95.3% of the dose points above the 10% isodose line passed the criteria of gamma that is less than one, given 3% dose difference (DD) or 3 mm distance to agreement (DTA). The disagreement comes from an intrinsic film dosimetry error (although this is a base of our comparative evaluation), an EPID modeling error, a dose reconstruction algorithm error, and a Monte Carlo calculation error. The pass rate was 99% between the reconstructed and forward doses, given 2% DD and 2 mm DTA (100%, given 3% DD and 3 mm DTA).

To quantitatively understand each error more in detail, the Monte Carlo code, XVMC, was commissioned to be within 1% difference from ion chamber measurements.[25] Film measurement showed 2% difference at beam axis (i.e., flat dose region) from forward Monte Carlo calculations in the same study. Therefore, the film error was estimated to be 3% as a maximum. Our calculational EPID model was determined to be accurate within 2% from EPID measurement.[28] This difference affected dose reconstruction accuracy because our algorithm utilizes calculated EPID response. The dose reconstruction algorithm itself is as accurate as forward MC calculation at beam axis (i.e., flat dose region), as it utilizes MC calculated responses. This was demonstrated in Fig. 5(e). As the algorithm utilizes MC calculations for responses, the above MC commissioning and EPID modeling errors (maximum 3%) affected the overall dose reconstruction error. The dose reconstruction error (containing evaluation near penumbra areas) was quantified among the central dose profiles in Fig. 5(e) compared with film measurement. Considering these individual sources of errors, the pass rate of the new method is

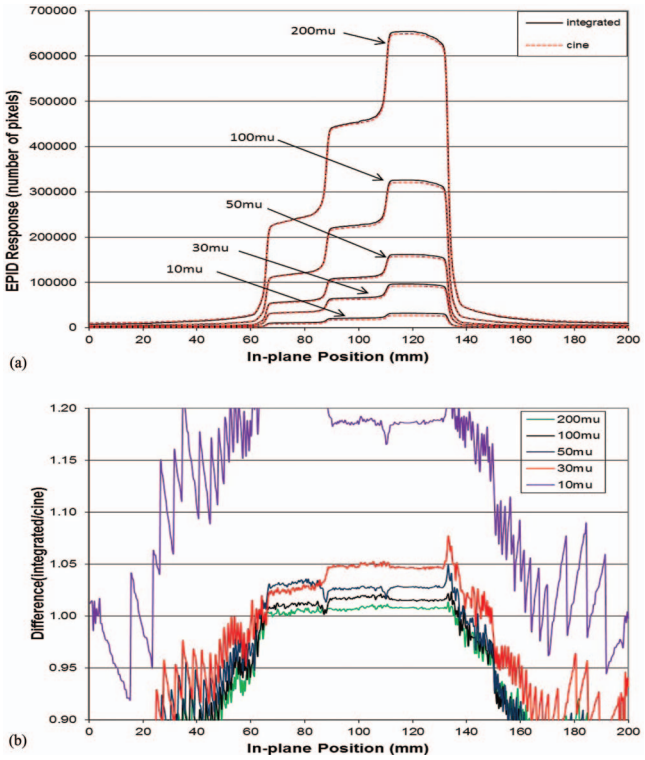

FIG. 6. (a) Beam profile comparison between integrated mode and cine mode for the test intensity-modulated beam in EPID at 150 cm. The cine mode data displayed above was determined after integration over time. (b) Relative difference showing ratio of integrated mode to cine mode.

reasonable validating the dose reconstruction method for the test beam used in this study. It is noteworthy that the original algorithm of dose reconstruction showed a higher 99.8% gamma pass rate given the criteria of 3% DD and 3 mm DTA, compared with film measurement, for a beam similar to the current test beam. The approximation in the derivation of the generalized response-based method of dose reconstruction may have led to the lower pass rate by 4.5%.

III.B. 4D dose reconstruction

III.B.1. Validation of EPID cine imaging

Figure 6 compares dose distributions between the cine (after integration over time) and integration modes of acquisition for the test beam irradiated with various MUs. The agreement was within 1% at the depth of dose maximum at 200 MU. The maximum difference of 18.6% was observed at 10 MU, the lowest MU, as listed in Table I. The discrepancy was variable with delivered MUs: it increased with decreasing MUs. This is believed to be due to beam instability at the start of acquisition and reading loss for the cine mode during MLC movement.[23] This shows limitations of the cine acquisition of step-and-shoot irradiation which need to be considered for future applications. More work on this aspect is necessary, but it is beyond the scope of this study. We have used 80 MUs

TABLE I. Response differences between integrated mode and cine mode for the test intensity-modulated beam with varying MUs. The differences were determined at the point of dose maximum.

MU	Difference (%)
10	18.6
30	4.6
50	2.8
100	1.5
200	0.8

TABLE II. Phase sorting of EPID images for four-dimensional dose reconstruction. EPID images acquired for the irradiation on the heterogeneous phantom were temporal-phase-sorted considering a single frame acquisition time of 0.0606 s, MLC travel duration of 0.85 s between segments, and phantom movement time of 4.5 s/cycle. Similar sorting was performed for the irradiation on the homogeneous phantom. Highlighted phases correspond to MLC travel duration.

Motion cycle	Phases (%)	Sorted image number	Subsum	Irradiation time (s)	Delivery time[a] (s)
1	10	7		0.42	0.42
	20	8	15	0.91	0.91
	30	7	22	1.33	1.33
	40	8	30	1.82	1.82
	50	7	37	2.24	2.24
	60	8	45	2.73	2.73
	70	7	52	3.15	3.15
	80	8	60	3.64	3.64
	90	7	67	4.06	4.06
	100	8	75	4.55	4.55
2	10	7	82	4.97	4.97
	20	8	90	5.45	5.45
	30				5.88
	40	1	91	5.52	6.36
	50	7	98	5.94	6.79
	60	8	106	6.42	7.27
	70	7	113	6.85	7.70
	80	8	121	7.33	8.18
	90	7	128	7.76	8.61
	100	8	136	8.24	9.09
3	10	7	143	8.67	9.52
	20	8	151	9.15	10.00
	30	7	158	9.58	10.42
	40	8	166	10.06	10.91
	50	7	173	10.48	11.33
	60	3	176	10.67	11.82
	70				12.24
	80	6	182	11.03	12.73
	90	7	189	11.45	13.15
	100	8	197	11.94	13.64
4	10	7	204	12.36	14.06
	20	8	212	12.85	14.55
	30	7	219	13.27	14.97
	40	8	227	13.76	15.45
	50	7	234	14.18	15.88
	60	8	242	14.67	16.36
	70	7	249	15.09	16.79
	80	8	257	15.58	17.27
	90	4	261	15.82	17.52
	100				

[a]Delivery time includes MLC travel time.

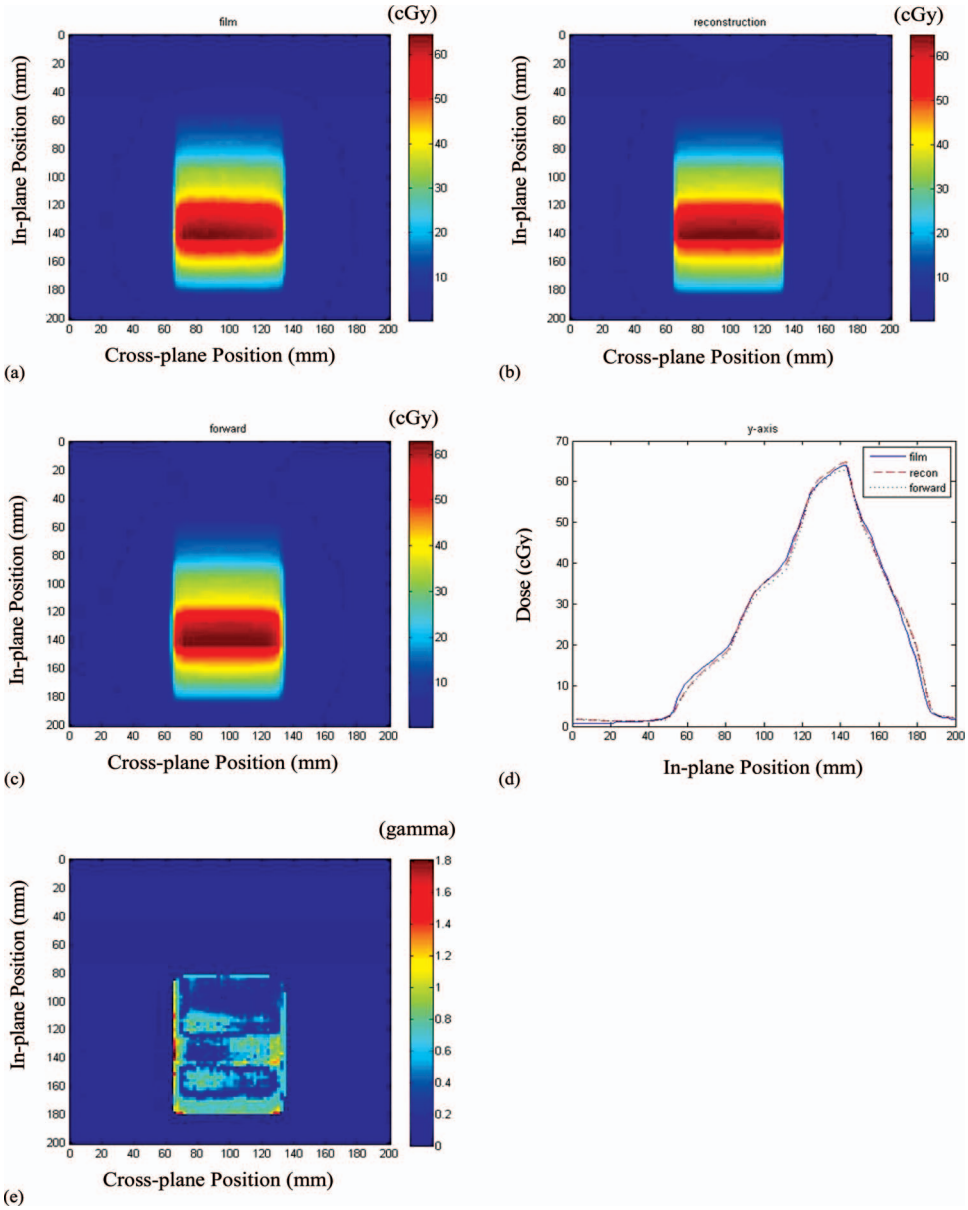

FIG. 7. (a) Dose profiles in cGy for the test IMRT beam measured with film on a midplane in the homogeneous flat phantom that was under motion, (b) dose profiles reconstructed at the same condition, (c) dose profiles forward-calculated at the same condition, (d) central dose profile comparison between the three at X = 100 mm, and (e) gamma comparison between dose profiles measured with film and reconstructed.

for all measurements in this study considering this discrepancy (2%) and film saturation. Such systematic discrepancy was corrected for in this study.

III.B.2. Dose reconstruction

Table II shows EPID image sorting to each temporal phase of radiation delivery. Through the evaluation of image acquisition time of each image (i.e., dicom header information), we could identify that 16 and 17 frames were acquired in a second implying that 1/16.5 or 0.0606 s was spent for a single image acquisition. Certain acquisition times were associated with a number of frames that are smaller than such number of frames per second. At these times, MLC traveled between segments, thereby stopping irradiation. The number of lacked frames was translated into the time spent for MLC travel, revealing that exactly 14 frames (0.85 s) were missing during each MLC travel. Note that the continuous scan is a mode of acquisition synchronized to beam pulses. Therefore, during the duration of no beam irradiation (MLC travel due to step-and-shoot irradiation) image acquisition did not occur, although the phantom moved. The phases associated with the MLC travel were identified and are highlighted in Table II and Fig. 4. For each temporal phase of image acquisition (4.5 s/10 phases or 0.45 s/phase), 7.4 frames (0.45 s/0.0606 s/frame) were approximately assigned. Therefore, we have assigned seven and eight frames alternatively from the first acquired image to each succeeding phase that is distributed throughout the entire beam delivery and the four cycles of the phantom motion. Table II shows the assigned image numbers and

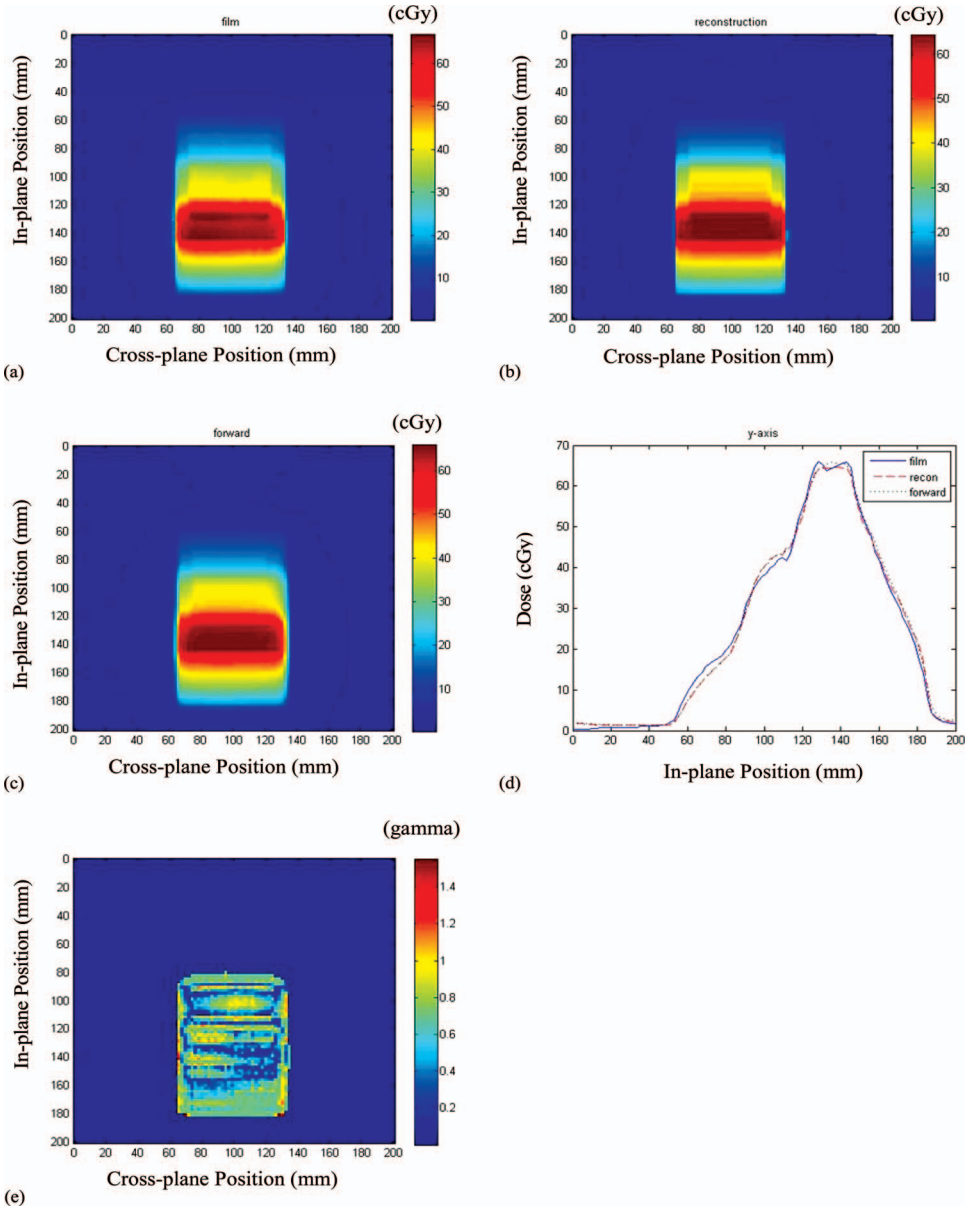

FIG. 8. (a) Dose profiles in cGy for the test IMRT beam measured with film on a midplane in the heterogeneous phantom that was under motion, (b) dose profiles reconstructed at the same condition, (c) dose profiles forward-calculated at the same condition, (d) central dose profile comparison between the three at X = 100 mm, and (e) gamma comparison between dose profiles measured with film and reconstructed.

irradiation and delivery times (MLC travel time inclusive) for each phase and cycle. In this process, we have skipped assigning or partially assigned the phases associated with the MLC travel. In total, 80 MU was delivered at 300 MU/min (or 5 MU/s). This corresponds to 16 s of irradiation time, if no dose rate fluctuation was assumed, during which the continuous images were acquired. This agreed with the total irradiation time of 15.82 s in Table II. The difference of 0.18 s comes from the assignment of 15 (7 + 8) frames per 2 phases rather than 14.8 frames (7.4 × 2) and imperfect beam stability during irradiation.

Figure 7 compares the reconstructed dose profile with the measured and the forward test beam delivered to the film and homogenous phantom in motion. In the comparison, 99.7% of dose points above 10% isodose line passed the criteria of gamma less than one, given 3% DD and 3 mm DTA. The agreement was acceptable, considering the above-discussed sources of errors and added sources: the use of a finite phase interval of 10% (despite continuous film movement with which the reconstructed dose is compared) for response calculation and dose reconstruction from cine images of EPID, minor image sorting error as discussed above, and the additional manual synchronization error discussed in Sec. II. The pass rate was 96.1% between the reconstructed and forward doses, given 2% DD and 2 mm DTA (99.8%, given 3% DD and 3 mm DTA). Note that the shape of the profile in Fig. 7(c) is different from that in Fig. 5(c) due to the motion of the phantom. The dose reconstruction calculation has involved 261 matrix calculations (equivalent to the number of the acquired cine images) and data processing using precalculated responses. This took 6 min. The calculation of virtual-beamlet responses spent approximately

8 s for each beamlet (0.5 × 0.5 cm) and a total of 53.3 min for the open field of 10 × 10 cm using dual six core 2.93 GHz Intel XEON CPUs and 12.0 GB RAM. A substantially faster calculation (13.3 min) was possible with a beamlet size of 1 × 1 cm, which still produced comparable pass rates lower by less than 1%. This calculation was performed for each phase for the heterogeneous case, constituting 10 calculations.

Figure 8 compares the reconstructed dose profile with the measured and the forwardly calculated profiles for the test beam that was delivered to the film and phantom in motion for the heterogeneous phantom. In the comparison, 96.4% of dose points passed the criteria of gamma less than one, given 3% DD and 3 mm DTA. The pass rate was 98.3% between the reconstructed and forward doses, given 2% DD and 2 mm DTA (100%, given 3% DD and 3 mm DTA).

IV. CONCLUSION

This study has proposed and validated a new, faster algorithm of inverse dose reconstruction that employs predetermined generalized dose responses and their ratio. Using predetermined dose responses and the new algorithm, numerous reconstruction processes that are equivalent to the number of continuously scanned EPID images were performed successfully and relatively quickly for 4D dose reconstruction. Therefore, this study has demonstrated the feasibility of 4D dose reconstruction using the continuous mode of image acquisition in EPID. This study finds its value as a first study on inverse 4D dose reconstruction that can be applicable to the validation of radiation delivery on moving organs (that includes various modern 4D delivery methods). Further studies include optimization of time interval for cine imaging, automated image sorting, and demonstration of 4D reconstruction on a humanoid phantom with more irregular breathing traces.

ACKNOWLEDGMENTS

Jong Oh Kim expresses gratitude to Dr. Fippel for providing him with the XVMC code. This study was in part supported by Varian Medical Systems, Inc.

[a]Author to whom correspondence should be addressed. Electronic mail: medicphys@hotmail.com; Telephone: 909 558 4820.

[1]P. J. Keall *et al.*, "The management of respiratory motion in radiation oncology," Med. Phys. **33**, 3874–3900 (2006).
[2]B. Yi, S. Han-Oh, B. L. Berman, F. Lerma, and C. Yu, "Real-time tumor tracking with preprogrammed dynamic multileaf collimator motion and adaptive dose-rate regulation," Med. Phys. **35**(9), 3955–3962 (2008).
[3]R. I. Berbeco, S. Nishioka, H. Shirato, G. T. Chen, and S. B. Jiang, "Residual motion of lung tumours in gated radiotherapy with external respiratory surrogates," Phys. Med. Biol. **50**, 3655–3667 (2005).
[4]G. D. Hugo, N. Agazaryan, and T. D. Solberg, "An evaluation of gating window size, delivery method, and composite field dosimetry of respiratory-gated IMRT," Med. Phys. **29**, 2517–2525 (2002).
[5]G. D. Hugo, N. Agazaryan, and T. D. Solberg, "The effect of tumor motion on planning and delivery of respiratory-gated IMRT," Med. Phys. **30**, 1052–1066 (2003).
[6]J. Duan, S. Shen, J. B. Fiveash, I. A. Brezovich, R. A. Popple, and P. N. Pareek, "Dosimetric effect of respiration-gated beam on IMRT delivery," Med. Phys. **30**, 2241–2251 (2003).
[7]R. George *et al.*, "Audio-visual biofeedback for respiratory-gated radiotherapy: Impact of audio instruction and audio-visual biofeedback on respiratory-gated radiotherapy," Int. J. Radiat. Oncol., Biol., Phys. **65**, 924–933 (2006).
[8]Y. Suh, E. Weis, H. Zhong, M. Fatyga, J. Siebers, and P. Keall, "A deliverable four-dimensional intensity modulated radiation treatment planning method for dynamic multileaf collimator tumor tracking delivery," Int. J. Radiat. Oncol., Biol., Phys. **71**(5), 1526–1536 (2008).
[9]M. Gui, Y. Feng, B. Yi, A. Dhople, and C. Yu, "Four-dimensional intensity-modulated radiation therapy planning for dynamic tracking using a direct aperture deformation (DAD) method," Med. Phys. **37**, 1966–1975 (2010).
[10]B. Cho, P. R. Poulson, A. Sloutsky, A. Sawant, and P. J. Keall, "First demonstration of combined KV/MV image-guided real-time dynamic multileaf-collimator target tracking," Int. J. Radiat. Oncol., Biol., Phys. **74**, 859–867 (2009).
[11]P. J. Keall *et al.*, "Geometric accuracy of a realtime target tracking system with dynamic multileaf collimator tracking system," Int. J. Radiat. Oncol., Biol., Phys. **65**, 1579–1584 (2006).
[12]A. Sawant *et al.*, "Management of threedimensional intrafraction motion through real-time DMLC tracking," Med. Phys. **35**, 2050–2061 (2008).
[13]B. C. Cho *et al.*, "A monoscopic method for real-time tumour tracking using combined occasional x-ray imaging and continuous respiratory monitoring," Phys. Med. Biol. **53**, 2837–2855 (2008).
[14]I. Yeo, J. Jung, and B. Yi, "Validation of amplitude and phase gating against potential irreproducibility of motion," Med. Phys. **36**, 2562 (2009).
[15]I. Yeo and L. An, "Verification of gated radiation therapy: Dosimetric shift and target coverage due to residual motion," Med. Phys. **35**, 2740 (2008).
[16]C. Chui, E. York, and L. Hong, "The effects of intra-fraction motion on the delivery of intensity-modulated field with a multileaf collimator," Med. Phys. **30**, 1736–1746 (2003).
[17]J. H. Kung, P. Zygmanski, N. Choi, and G. T. Y. Chen, "A method of calculating a lung clinical target volume DVH for IMRT with intrafractional motion," Med. Phys. **30**, 1103–1109 (2003).
[18]D. Litzenberg, S. Hadley, N. Tyagi, J. Balder, R. Ten Haken, and I. Chetty, "Synchronized dynamic dose reconstruction," Med. Phys. **34**, 91–102 (2007).
[19]B. M. C. McCurdy, K. Luchka, and S. Pistorius, "Dosimetric investigation and portal dose image prediction using an amorphous silicon electronic portal imaging device," Med. Phys. **28**, 911–924 (2001).
[20]T. R. McNutt, R. R. Mackie, P. Reckwerdt, N. Papanikolaou, and B. R. Paliwal, "Calculation of portal dose using the convolution/superposition method," Med. Phys. **23**, 527–535 (1996).
[21]S. M. Nijsten, A. W. Minken, P. Lambin, and I. A. Bruinvis, "Verification of treatment parameter transfer by means of electronic portal dosimetry," Med. Phys. **31**, 341–347 (2004).
[22]K. L. Pasma, B. J. M. Heijmen, M. Kroonwijk, and A. G. Visser, "Portal dose image (PDI) prediction for dosimetric treatment verification in radiotherapy. I. An algorithm for open beams," Med. Phys. **25**, 830–840 (1998).
[23]B. M. C. McCurdy and P. B. Greer, "Dosimetric properties of an amorphous-silicon EPID used in continuous acquisition mode for application to dynamic and arc IMRT," Med. Phys. **36**, 3028–3039 (2009).
[24]S. Han-Oh, B. Yi, F. Lerma, M. Gui, C. Yu, and B. Berman, "Verification of MLC based real-time tumor tracking using an electronic portal imaging device," Med. Phys. **37**, 2435–2440 (2010).
[25]I. J. Yeo, J. W. Jung, M. Chew, J. O. Kim, B. Wang, S. DiBiase, Y. Zhu, and D. Lee, "Dose reconstruction for intensity-modulated radiation therapy using a non-iterative method and portal dose image," Phys. Med. Biol. **54**, 5223–5236 (2009).
[26]J. J. Sonke, L. Zijp, P. Remeijer, and M. van Herk, "Respiratory correlated cone beam CT," Med. Phys. **32**, 1176–1186 (2005).
[27]J. V. Siebers, J. O. Kim, L. Ko, P. J. Keall, and R. Mohan, "Monte Carlo computation of dosimetric amorphous silicon electronic portal images," Med. Phys. **31**, 2135–2146 (2004).
[28]J. W. Jung, J. O. Kim, I. J. Yeo, Y.-B. Cho, S. M. Kim, and S. DiBiase, "Fast transit portal dosimetry using density-scaled layer modeling of aSi-based electronic portal imaging device and Monte Carlo method," Med. Phys. **39**, 7593–7602 (2012).
[29]I. Yeo and J. Kim, *A Procedural Guide to Film Dosimetry: With Emphasis on IMRT* (Medical Physics, Madison, 2004).
[30]M. Fippel, "Fast Monte Carlo dose calculation for photon beams based on the VMC electron algorithm," Med. Phys. **26**, 1466–1475 (1999).